IEEE Access
Multidisciplinary ⋮ Rapid Review ⋮ Open Access Journal

Received October 29, 2021, accepted November 14, 2021, date of publication November 18, 2021,
date of current version December 2, 2021.

Digital Object Identifier 10.1109/ACCESS.2021.3129180

The Impact of the Control Strategy in Flux Observer Based Sensorless Control of Synchronous Reluctance Motors

ANDREA CREDO, LINO DI LEONARDO, FRANCESCO PARASILITI COLLAZZO, AND MARCO TURSINI, (Member, IEEE)
Department of Industrial and Information Engineering and Economics, University of L'Aquila, 67100 L'Aquila, Italy
Corresponding author: Andrea Credo (andrea.credo@univaq.it)

ABSTRACT This paper compares different control strategies of the synchronous reluctance motor to outline their impact on the accuracy of flux-observer based sensorless operation. Maximum torque per ampere, maximum efficiency, and maximum power factor controls, usually referred to optimize the operating performance of synchronous reluctance motors are considered. Alternative solutions not usual in literature but specifically investigated for supporting the estimation are also considered, namely constant direct-axis-current and constant direct-axis-flux controls. The flux-observer detects the flux components in the two-phase stationary reference frame by a non-linear model achieved by finite-elements computations. An auxiliary mechanical observer who accounts for the finite-elements mapping of the torque is adjusted by the flux estimation error and provides the rotor position and speed needed for sensorless control. An extended set of experimental tests is presented where the different control methods are compared in terms of position and speed estimation errors and overall control quality. A four poles, three kW synchronous reluctance prototype designed for general industry application is used for testing.

INDEX TERMS Synchronous reluctance motor, sensorless control, flux-observer, finite elements modelling, current control strategies.

I. INTRODUCTION

Synchronous reluctance (SynRel) motors are going to play an important role among AC drives for the foreseeable future, as already highlighted since several decades [1], [2]. In fact they feature higher acceleration capability compared to the other AC motors due to the lower inertia, a good power-to-weight ratio, and extended flux-weakening operation, all characteristics that match the requirements of prominent industrial and transportation applications [3]–[6].

The torque production of the SynRel only depends on the level of magnetic anisotropy that characterizes the shape of the rotor. This could be a limitation compared to motors with independent excitation sources such as permanent magnets (PM). Nevertheless, the advances in electromagnetic design achieved by the use of powerful Finite Elements (FE) tools, combined with sophisticated optimization algorithms, allow the design of high anisotropy shapes and the achievement of performance very close to that of PM motors [7]–[10].

But another aspect is often invoked as one of the factors limiting the diffusion of the SynRel: the complexity in control. In fact, these machines have intrinsically nonlinear features, including saturation and cross-coupling effects, strictly related to the specific rotor structure. These matters prevent the standardization of the drives and must be carefully taken into account to fit the control requirements. Moreover, the relationship between the torque and the current is quadratic, which makes it difficult the design of the control loops [11]–[14].

On the other hand, the presence of a salient rotor is an advantage for sensorless control, [15]. In fact, custom approaches to rotor position and speed detection such as signal-injection techniques can be used, in which high-frequency test signals are superimposed on the fundamental supply and their effects are processed in a closed-loop scheme [16], [17]. Unfortunately, signal-injection techniques suffer for un-modeled saturation and cross-couplings which

The associate editor coordinating the review of this manuscript and approving it for publication was Zhuang Xu.

affect the saliency ratio; moreover, filtering actions are involved which makes it hard to operate when the speed increases.

Model based flux-observers can be combined with signal-injection techniques to benefit from their respective good performance in the high and low speed ranges, [18]–[20]. To improve the accuracy of the estimation, especially at low-speed operation, FE mapped flux models [21], or self-commissioning techniques [22], [23] can be used. Kojima *et al.* [24] introduce a correction factor that takes into account the machine saturation and a torque-dependent gain to correct the position error.

Despite many aspects of the sensorless control of SynRel motors have been treated, the impact of the control strategy pursued in field-orientation has not yet been adequately investigated. Depending on the application and/or the operating torque-speed range, different Optimum Control (OC) strategies are used, some of them analytically definable in linear flux-current hypothesis such as Maximum Torque per Ampere (MTPA), Maximum Torque per Flux (MTPF), and Maximum Power Factor (MPF), mostly implemented in terms of $d-q$ current components, Figure 1, [12], [25].

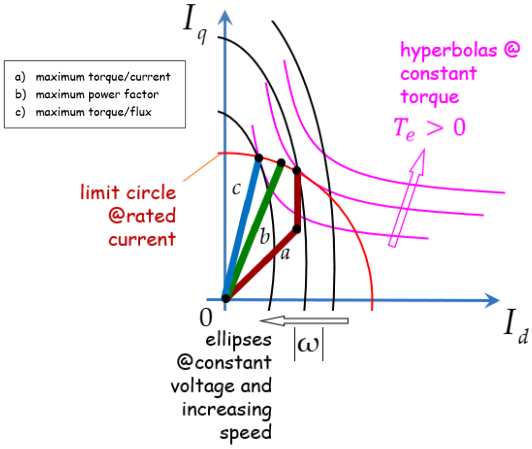

FIGURE 1. Optimum control strategies of a SynRel motor.

The use of a certain control strategy rather than another affects the magnetization state of the machine in a different way, both statically and dynamically. Therefore, it stands to reason that this selection affects the quality of the estimation and the sensorless control. This paper investigates such a matter.

The sensorless control scheme based on flux-observer originally presented in [26] is considered and experimentally analyzed in terms of speed and rotor position estimation and control quality. Signal injection is omitted to simplify the study. Both speed reversion and a proper sinusoidal-speed test are used for the sake of dynamic robustness analysis. Optimum control strategies such as MTPA, Maximum Efficiency (ME), and MPF are compared with a couple of alternative solutions specifically conceived for improving the estimation performance, namely constant d-axis flux (CDAF) and constant d-axis current (CDAC) controls.

The sensorless algorithm uses the combination of a flux observer and a mechanical observer in order to increase the low-speed area in which observer-based sensorless approaches usually suffer. The flux observer estimates the components of the flux vector in the two-phase stationary reference frame according to a non-linear model achieved by finite-elements computations. An auxiliary mechanical observer adjusted by the flux estimation errors provides the rotor position and speed needed for sensorless.

The paper is organized as follows: Section II describes the SynRel flux model and illustrates its characteristics for the considered motor prototype; for a better understanding of the study, the flux and mechanical observers are recalled in Section III, with the sensorless control scheme; the different control strategies are presented in Section IV; Section V presents and discusses the experimental results obtained by the different current control strategies; finally, the concluding remarks are summarized in Section VI.

II. FLUX MODEL CHARACTERIZATION

The accurate modeling of the electromagnetic behavior is an essential requirement in flux observers for SynRel motors. This can be done clearly and effectively through the relationships between the current and flux vectors components in the rotor-fixed $d-q$ reference frame, Figure 2.

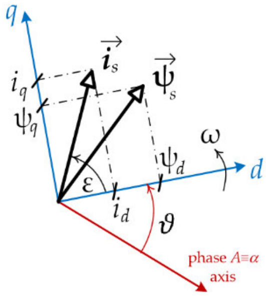

FIGURE 2. Flux and current space vectors in a SynRel motor.

In a basic representation, it is usual to express these relations as $\psi_d = L_d i_d$ and $\psi_q = L_q i_q$, where ψ_d and ψ_q are the axes flux linkages, i_d and i_q are the axes currents, and L_d and L_q are the $d-q$ axes inductances. Note that by aligning the d-axis with the highest permeance rotor axis, it follows $L_d > L_q$.

Actually, the load/speed operating range involves highly variable levels of flux, current, and frequency. As a consequence, the motor electrical parameters cannot be considered constant. As far as the inductances are concerned, the availability of quite reliable analysis tools such as FEs allows the individuation of the flux vs. current relation with much more accuracy, including saturation and mutual ‘‘cross-couplings’’ effects between the d-and q-axis fluxes.

Hence, a more realistic non-linear model taking into account these effects must be considered, where the flux-to-current relationships are expressed in the general form:

$$\psi_d = \psi_d\left(i_d, i_q\right) \tag{1}$$

$$\psi_q = \psi_q\left(i_d, i_q\right) \tag{2}$$

and must be evaluated for each machine design.

In this study a 3 kW SynRel motor prototype has been considered, designed with four flux barriers on the rotor, Figure 3. It has been conceived having the same stator windings and the same housing of a standard 3 kW induction motor for industrial application. Motor parameters and the ratings at base operating point are shown in Table 1.

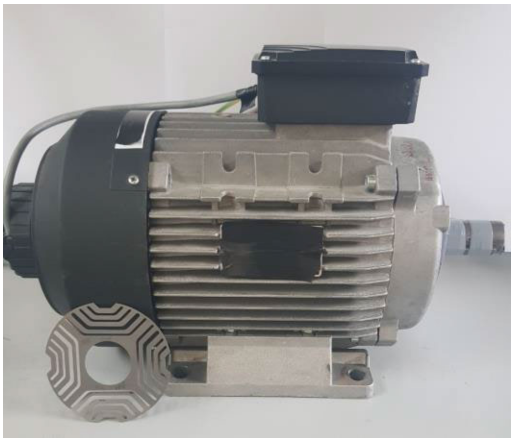

FIGURE 3. SynRel motor prototype: rotor core and assembled machine.

TABLE 1. Main data of the SynRel motor.

Values @ rated operating condition	
phase voltage	$\hat{V}_n = 220 \times \sqrt{2}\, V_{pk}$
phase current	$\hat{I}_n = 10.67\, A_{pk}$
direct current	$\hat{I}_{dn} = 3.93\, A_{pk}$
quadrature current	$\hat{I}_{qn} = 9.92\, A_{pk}$
direct flux	$\hat{\psi}_{dn} = 0.87\, V_{pk}s$
speed	$n_n = 1500\, rpm$
power	$P_n = 3.142\, kW$
torque	$T_{en} = 20\, Nm$
Parameters	
number of pole pairs	$p = 2$
direct inductance*	$L_d = 186\, mH$
quadrature inductance*	$L_q = 34.1\, mH$
phase resistance	$R = 1.975\Omega\ @20°C$
Base per-unit system	
current	$I_B = \hat{I}_n$
flux	$\psi_B = 0.98\, V_{pk}s$
speed	$n_B = n_n$
torque	$T_{eB} = 30.3\, Nm$

* At rated operating condition.

The rotor shape has been designed using a FE tool interfaced with an optimization algorithm whose goals were: 1^{st}) maximizing the power factor at the base speed; and 2^{nd}) minimizing the torque ripple in the meanwhile, [27].

The flux-to-current functions (1) and (2) have been obtained by processing the two-dimensional model provided by the FE tool once the optimization goals were reached. Their behaviours are shown in Figures 4 and 5: the cross-coupling between the $d - q$ axes and the saturation effects are clearly accounted.

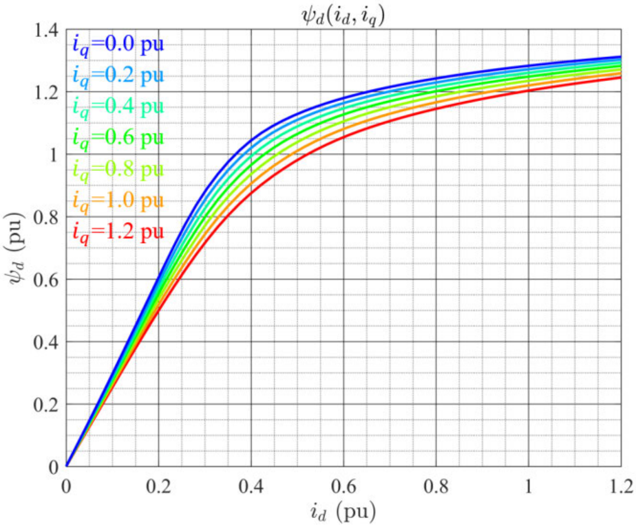

FIGURE 4. Direct-axis flux vs. *d-q* currents.

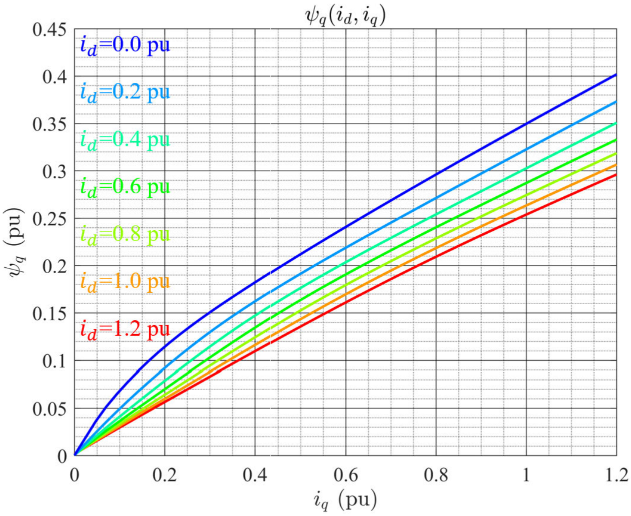

FIGURE 5. Quadrature-axis flux vs. *d-q* currents.

The proposed mechanical observer (see next section) needs the motor torque as a system input. The electromagnetic torque depends on the flux and current components by the general expression:

$$T_e = \frac{3}{2} p \left(\psi_d i_q - \psi_q i_d\right) \tag{3}$$

In theory, it can be calculated by substituting the fluxes functions (1) and (2) achieved by the FE calculation in equation (3) (indirect computation). Actually, experiences show that greater accuracy is achieved if the torque is calculated as direct function of the axis currents (direct computation), i.e.:

$$T_e = T_e\left(i_d, i_q\right) \tag{4}$$

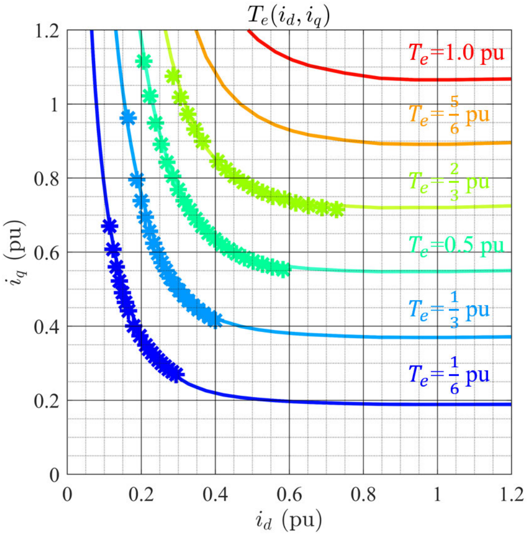

FIGURE 6. Constant torque loci vs. *d-q* currents.

Figure 6 shows the constant torque loci for the SynRel prototype considered in this study. Comparison with experimental tests (labeled with stars in the figure) confirms the accuracy of the direct computation vs. the indirect one.

III. FLUX OBSERVER-BASED SENSORLESS CONTROL

Flux observers use the error between the fluxes (indirectly identified) and the observed ones to calculate the rotor speed and angular position, directly or through related variables, [28], [29]. Being model-based method, flux observers are sensitive to measurement noise, parameters variation and model inaccuracy, several authors explain the importance of estimating the stator phase resistance too, [30]–[32]. Moreover, the flux level in SynRels is strictly related to the load conditions and often subject to fast changing.

For these reasons and the intrinsic electromagnetic nonlinearities, the use of flux-observers for sensorless control in SynRels is challenging. Particularly flux observers including non-linear flux-current relations have been proposed since the early 1990s to improve the control accuracy, [33], [34].

The algorithm considered for this study was originally presented in [26]. It combines two kinds of observers: a flux observer (main observer) and a mechanical one (auxiliary observer). The flux observer calculates the axis flux components of the machine using the difference between its output ("observed flux") and the estimation of the actual flux ("estimated flux"); the mechanical observer uses a proper arrangement of the flux correction feedback to calculate the mechanical variables, namely rotor speed and d-axis position, needed to close the sensorless control. Both the electrical and mechanical equations of the machine are used to these purposes.

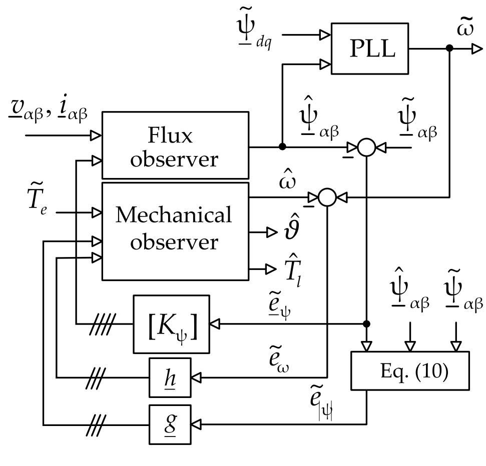

FIGURE 7. The proposed flux & mechanical observers.

The whole scheme is shown in Figure 7, where symbols with a caret (^) indicate the observed values while those with a tilde (∼) indicate the estimated ones.

Based on the voltage balance of the equivalent stator-fixed $\alpha - \beta$ windings:

$$\frac{d\underline{\psi}_{\alpha\beta}}{dt} = \underline{v}_{\alpha\beta} - R\underline{i}_{\alpha\beta} \tag{5}$$

the flux observer is arranged as:

$$\frac{d\hat{\underline{\psi}}_{\alpha\beta}}{dt} = \underline{v}_{\alpha\beta} - R\underline{i}_{\alpha\beta} + \left[K_\psi\right]\tilde{\underline{e}}_\psi \tag{6}$$

where $\underline{v}_{\alpha\beta} = [v_\alpha v_\beta]^T$ and $\underline{i}_{\alpha\beta} = [i_\alpha i_\beta]^T$ are the vectors of the voltage and current components, respectively known and measured system inputs, R is the phase-windings resistance, $\tilde{\underline{e}}_\psi = \hat{\underline{\psi}}_{\alpha\beta} - \tilde{\underline{\psi}}_{\alpha\beta} = [\hat{\psi}_\alpha - \tilde{\psi}_\alpha \hat{\psi}_\beta - \tilde{\psi}_\beta]^T$ is the flux estimation error, and $\left[K_\psi\right]_{2\times 2}$ is the gains matrix of the flux-observer. It should be noted that the estimation error is built with the estimated quantity, since the flux measurement is not available.

The matrix $\left[K_\psi\right]$ can be computed as proposed in [35], choosing the structure $[K] = k[I]$, $k > 0$ for stability, and assuming the estimated flux equal to the actual one. The $\alpha - \beta$ observed and $d - q$ estimated flux components allow the calculation of the rotor d-axis estimated speed $\tilde{\omega} = d\tilde{\vartheta}\big/dt$ by a quadrature "*sin/cos*" phase-locked loop (PLL) algorithm, being:

$$\tilde{\vartheta} = \arccos\frac{\hat{\underline{\psi}}_{\alpha\beta}\cdot\tilde{\underline{\psi}}_{dq}}{\sqrt{\left|\hat{\underline{\psi}}_{\alpha\beta}\wedge\tilde{\underline{\psi}}_{dq}\right|^2 + \left(\hat{\underline{\psi}}_{\alpha\beta}\cdot\tilde{\underline{\psi}}_{dq}\right)^2}} \tag{7}$$

the estimated rotor d-axis position ($\wedge$ and $\cdot$ indicate the vector and dot product respectively).

The difference $\tilde{e}_\omega = \hat{\omega} - \tilde{\omega}$ between the observed speed $\hat{\omega}$ and the estimated one is the speed estimation error used to correct in feedback the auxiliary mechanical observer.

The mechanical observer is arranged as a state-and-disturbance observer to comply with the presence of the unknown load-torque. It has the following form:

$$\hat{\underline{x}}_m = \int \left([A]\,\hat{\underline{x}}_m + \underline{b}\tilde{T}_e + +\underline{g}\tilde{e}_\omega + \underline{h}\tilde{e}_{|\psi|} \right) dt \tag{8}$$

where $\hat{\underline{x}}_m = \left[\hat{\omega}\ \hat{\vartheta}\ \hat{T}_l\right]^t$ is the vector of the extended mechanical observed states, namely rotor speed $\hat{\omega}$, rotor position $\hat{\vartheta}$, and load torque $\hat{T}_l$, the latter represented for the computation by a zero derivative dynamic model, $\tilde{T}_e$ is the estimated motor torque (considered as a system input), $[A]$ and $\underline{b}$ the matrix and vector of the mechanical parameters,

$$[A] = \begin{bmatrix} 0 & 0 & -p/J \\ 0 & 1 & 0 \\ 0 & 0 & 0 \end{bmatrix};\ \underline{b} = \begin{bmatrix} p/J \\ 0 \\ 0 \end{bmatrix} \tag{9}$$

with J inertia of the rotating masses and p the pole pairs number, $\tilde{e}_\omega$ and $\tilde{e}_{|\psi|}$ the speed and flux-amplitude estimation errors, the latter arranged as:

$$\tilde{e}_{|\psi|} = sign\left(\left|\tilde{\psi}_{\alpha\beta}\right| - \left|\hat{\psi}_{\alpha\beta}\right|\right)\left|\tilde{\underline{e}}_\psi\right| \tag{10}$$

being $\left|\tilde{\psi}_{\alpha\beta}\right|$, $\left|\hat{\psi}_{\alpha\beta}\right|$, and $\left|\tilde{\underline{e}}_\psi\right|$ the amplitudes (moduli) of the estimated flux vector, the observed flux vector, and the flux estimation error vector, respectively.

Finally, $\underline{g} = [g_1 g_2 g_3]^T$ and $\underline{h} = [h_1 h_2 h_3]^T$ are the gains vectors of the mechanical observer. Assuming the estimated speed and torque (provided by the flux observer) equal to the actual ones, $g = [g_1\ 0\ 0]$ and $h = [0\ 0\ h_3]$ are chosen, with $g_1 > 0$ and $h_3 > 0$ for the system stability.

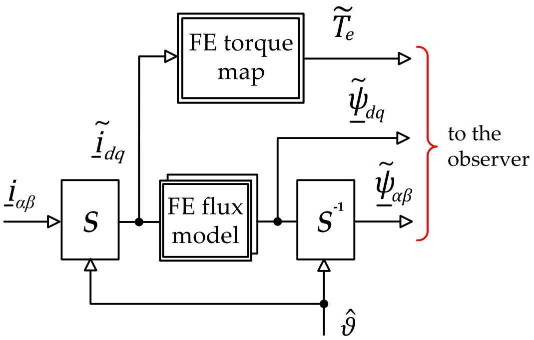

FIGURE 8. FE-based flux model and torque map.

The estimated variables needed to compute the observers are obtained by means of the flux model and the torque calculation as shown in Figure 8. Both are evaluated in the $d-q$ reference frame, according to the functions (1), (2) and (4) achieved by the FE model analysis to take into account flux saturation and cross-coupling effects.

Thereafter, both direct and inverse Park transformations are needed in the scheme. Notice that the Park transformation is computed by the observed rotor angle $\hat{\vartheta}$:

$$\left[S(\hat{\vartheta})\right] = \begin{bmatrix} \cos\hat{\vartheta} & \sin\hat{\vartheta} \\ -\sin\hat{\vartheta} & \cos\hat{\vartheta} \end{bmatrix} \tag{11}$$

The look-up-tables (LUTs) for the flux model can be also obtained through an elaborated self-commissioning sequence (which can be more practical) as presented in [36]. Considering the development of the SynRel and its possible adoption in application aimed to the mass production, the solution based on FEM is suitable.

The sensorless speed control scheme based on the flux observer is shown in Figure 9. It allows operation in the constant torque range (the study of flux weakening performances is beyond the scope of this paper).

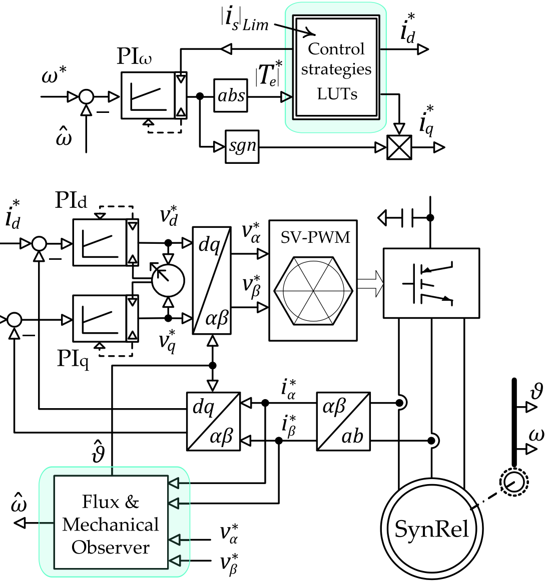

FIGURE 9. Sensorless control scheme.

The flux and mechanical observers provide the rotor d-axis position and speed control feedbacks. The observed position is used for the field orientation of the inner current loops and the speed feedback to close the outer speed control loop. Both the speed and the current loops are implemented by standard proportional-integral PI regulators with output limitation and anti-wind-up, while the voltage-source inverter is modulated by a space-vector algorithm. A circular limitation is implemented for the voltage reference.

The speed regulator outputs the torque reference T_e^* which provides the commands of the current loops, namely i_d^* and i_q^* according to the selected control strategy. The control strategies are mapped in LUTs obtained by FE model analysis. In order to have the same mechanical dynamics with the different control strategies considered in this study, providing that the control input is a torque command (see Figure 9), the FE LUTs are built to produce, with any given strategy, the current commands which give the same torque requested by the PI speed regulator. Moreover, the maps provide the torque reference limit according to the selected current limit. Alternatively, the same torque limit can be imposed for all control strategies.

IV. CURRENT CONTROL STRATEGIES

Different kinds of current control strategies were implemented and compared to verify their effects on the estimation quality of the observer, in particular speed and position estimation errors, and the consequent impact on overall control accuracy. Each strategy corresponds to a given trajectory on the $d-q$ currents plane.

The first group includes those controls conceived to maximize the performance of the motor and/or drive system and specifically: maximum torque per ampere (MTPA), maximum efficiency (ME), and maximum power factor (MPF), [37]–[39].

MTPA control is the standard choice for SynRel operation in the constant torque region. It minimizes the Joule losses and thus provides a good motor efficiency. Its trajectory on the $d-q$ currents plane is the locus of the points closest to the origin on each constant torque hyperbola.

ME control minimizes the motor losses, included the frequency dependent iron losses. For this reason, it depends also on the speed and requires a 2-D table to be implemented. Due to manufacturing inaccuracy, experimental evaluation is almost inevitable.

MPF control reduces the reactive power engaged, increasing the current and reducing the voltage. It is an interesting strategy for the SynRel as the power factor of this motor is inherently low. It slightly depends on the speed value and can be well approximated by a single trajectory in the $d-q$ currents plane.

Figure 10 shows the trajectories of these controls for the considered prototype (in case of ME and MPF the curves refer to the rated speed of the machine). Both FE calculations and experimental measurements are shown, testifying the excellent degree of accuracy of the FE modeling.

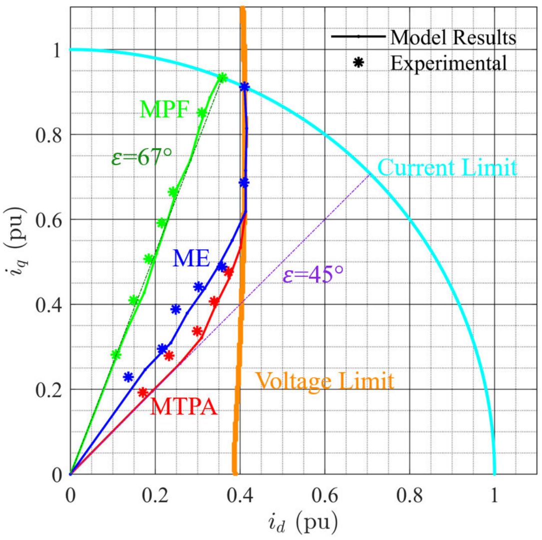

FIGURE 10. MTPA, ME and MPF control trajectories.

Notice that at low d-current values, when saturation is still not reached, the MTPA trajectory matches well that provided by the linear model of the machine, usually expressed in terms of the angle ε between the current space vector and the d-axis (see Figure 2). This is even more true for the MPF, which spans for lower d-current values. Then, MTPA can be approximated by setting $\varepsilon = 45°$ ($i_d = i_q$), while the MPF control by setting $\varepsilon = arctan \sqrt{L_{d,b}/L_{q,b}} \cong 67°$.

Basically, all the controls conceived to maximize the performance reduce the currents and hence the flux when the load reduces: MTPA, ME and MPF trajectories tend toward the origin of the $d-q$ currents plane, i.e., currents and flux tend to zero at the limit.

Unfortunately, sensorless controls based on flux observers are sensitive to the flux variation and suffer at low level of signals. Therefore, control strategies that does not exceed a certain lower flux threshold can increase the quality of the control, [40].

To verify this hypothesis, alternative controls are conceived and tested, namely: constant d-axis flux (CDAF) and constant d-axis current (CDAC). Figure 11 shows the trajectories of the second group of strategies for the tested prototype. In addition to the curves at the rated conditions, those at half of the rated values were considered (the latter assuming to average with respect to the possible load conditions).

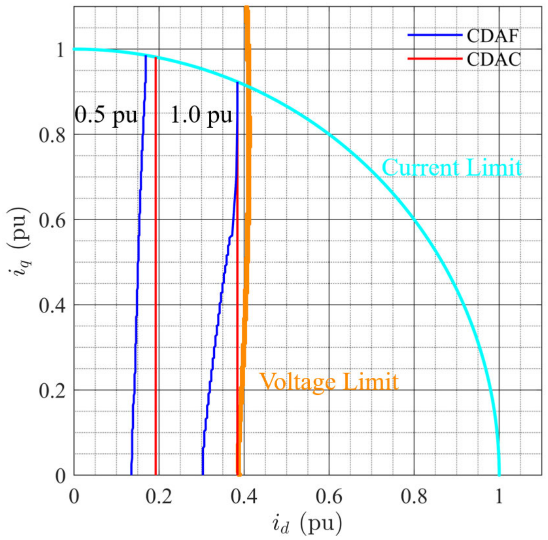

FIGURE 11. CDAF, CDAC (left) (right) control trajectories.

V. EXPERIMENTAL RESULTS

In the experimental set-up, the motor is fed by an IGBT inverter running at 10 kHz PWM frequency, while the control module is based on a TMS 320F28379S micro-controller equipped with a large flash memory of up to 1024 kilobytes. The latter feature is needed to store the high resolution LUTs involved in the observer as well as in the control strategies.

The experimental facility and the motor test bench are shown in Figure 12. The micro-controller is interfaced with the host computer by a fast serial-link allowing real-time (460800 baud rate) data acquisition and display of control variables through MATLAB/Simulink. The SynRel prototype is equipped with a 2048 PPR incremental encoder for

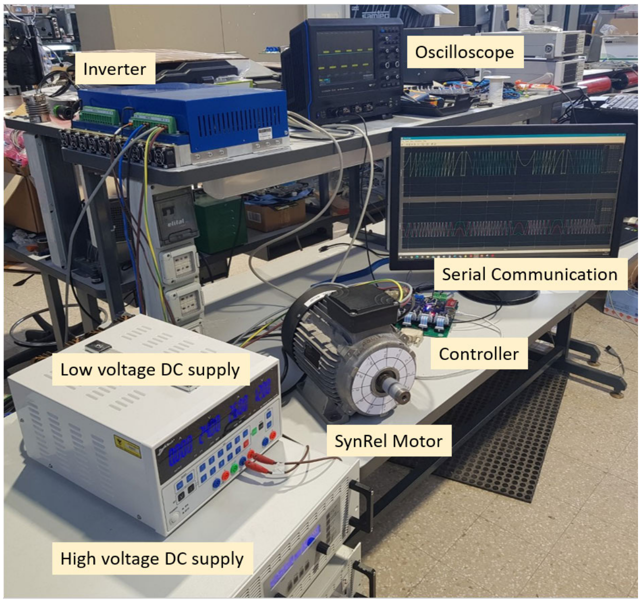

FIGURE 12. Motor test bench (left) and drive system (right).

debugging the sensorless control (by the measurement of the actual position, speed, and $d-q$ currents) and for sensored operation.

The experimental tests concerned the operation of the sensorless control scheme at no load with a sinusoidal speed command of proper period and amplitude. A short video of the tests is shown in [41]. The type of test was conceived to yield the worst working conditions for the flux observer, such as low speed and reversion. Particularly, at no-load the flux is forced to oscillate around its minimum value which is different for the two groups of strategies: zero for the MTPA, ME and MPF, not zero for the CDAF and CDAC. Furthermore, the algorithm of the mechanical observer is simplified at no-load, allowing a clearer interpretation of the results.

Preliminary tests in sensored operation allowed to properly select period and amplitude of the sinusoidal reference. Figure 13 shows the speed-torque trajectories for some of these experiments (the torque is computed by the FE maps and MTPA control is used).

After some evaluations an amplitude of 300 rpm (0.2 $p.u.$) with a relatively large period of 4 s has been chosen, which involves a peak torque of about 0.8 Nm. In this speed range, the speed-dependent ME trajectories are practically superposed and very close to the MTPA curve. Thereafter, it is reasonable to use the same curve for the two controls.

Figures 14 and 15 show the results of MTPA/ME, and MPF controls in sensorless operation. The observer gains are set to $k = 0.004$, $g_1 = 0.01$, and $h_3 = 0.012$, values used for all the control strategies considered in the paper for the sake of comparison (the corresponding bandwidth is about 6.4 Hz).

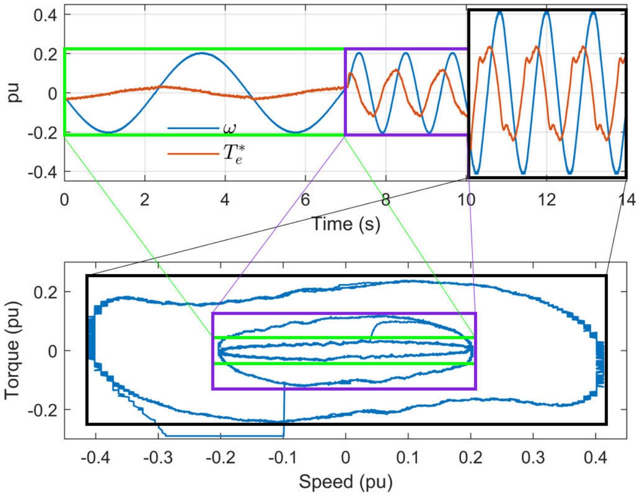

FIGURE 13. Torque-speed trajectories with different amplitude and period of the sinusoidal speed reference.

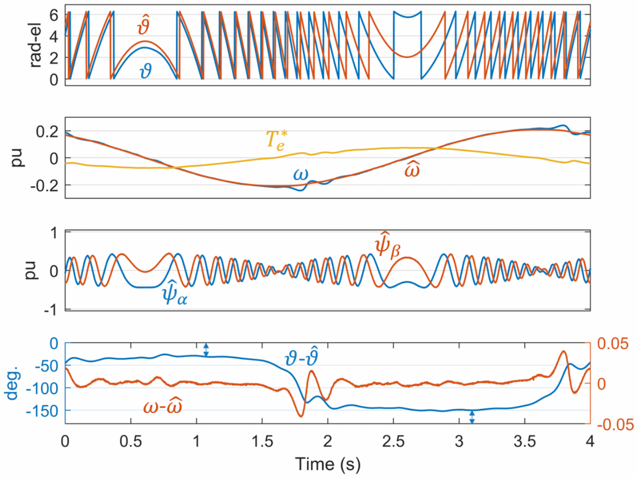

FIGURE 14. MTPA/ME controls.

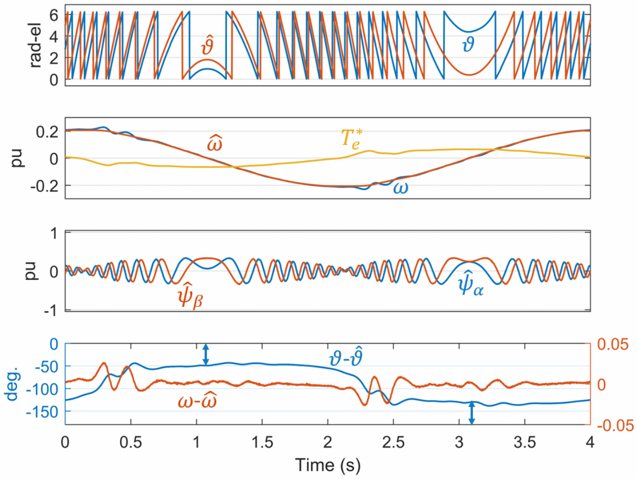

FIGURE 15. MPF control.

Speed control is maintained both with MTPA/ME and with MPF cases, but the position error is very large, between 30 and 40 deg. in absolute value (respect zero or ±180 degrees, which are equivalent equilibrium positions in a SynRel). The quality of the current control is strongly

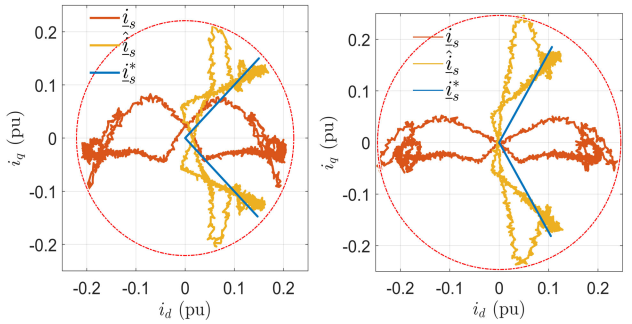

FIGURE 16. MTPA/ME (left) and MPF (right) control loci.

affected by the large position error as clearly visible by the current loci in Figure 16 and the time waveforms in Figure 17. What is evident is the discontinuity triggered by the zero-flux condition which affects the speed estimation and causes the reversion of the position estimate from the first (zero) to the others (±180 deg.) equilibrium positions.

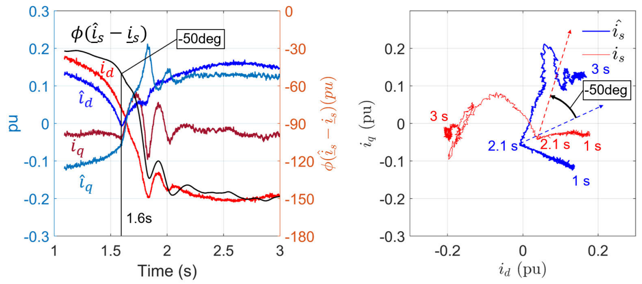

FIGURE 17. MPF control details.

The comparison between MTPA/ME and MPF shows lower transient effects of the zero-flux discontinuity on the speed error for MPF. This is due to the switching between close estimated positions, that is paradoxically higher position errors to the respective equilibrium position are favorable to this extent. Really, the actual current in MPF detuned control spans for lower torque values respect to MTPA/ME, hence the dynamic stress on the control is lower.

Figures 18 and 19 show the results of CDAF and CDAC control at 50% of the rated d-flux and d-current values respectively.

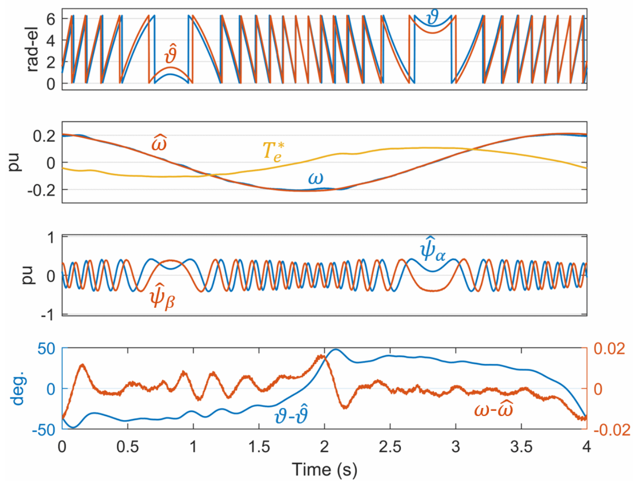

FIGURE 18. CDAF control at 50% of rated value.

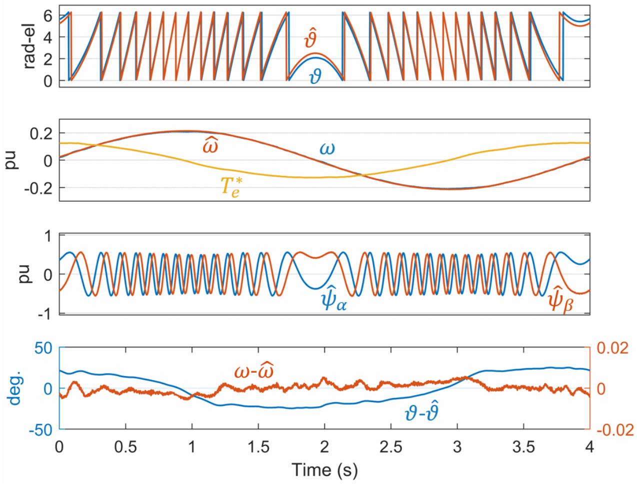

FIGURE 19. CDAC control at 50% of rated value.

Speed control is maintained in both the cases, the position estimation error is still very large for CDAF (up to 47 deg.) while is significantly lower for the CDAC (25 deg.), similarly the speed error is lower for the CDAC (not exceeding 5% of the commanded speed). The minimum flux operation (that occurs at zero crossing of the torque command) triggers a change of sign of the position estimation error and the following transient yields the maximum peak errors. But the position estimate does not reverse the equilibrium position (equal to zero in the shown tests), and this is an evidence of better convergence characteristics respect to the MTPA/ME and MPF controls, which can be correlated to the absence of zero-flux operation. The overall results are better than with the MTPA/ME and MPF controls and confirm the assumption that providing a minimum flux/current level improves the flux-observer-based estimation. In fact, the CDAC control performs better than CDAF as it works in a higher flux range. Especially the CDAC control quality is not far from what expected in a sensorless application.

Finally, Figures 20 and 21 show the results of the CDAF and CDAC control at rated 100% d-flux and d-current values, respectively. In these cases, the controls perform in flux ranges almost doubled respect to the 50% cases, again with the CDAC flux greater than CDAF.

The position estimation error assumes a sinusoidal shape with maximum error of 11 deg. for the CDAF and 8.5 deg. for the CDAC. The speed error is low, not exceeding 2.5% of the commanded speed for both the controls. The current control quality is clearly improved also respect to the 50% cases, as shown in Figure 22 and 23: now the controlled current components are very close to the actual ones, especially as for the current control angle is concerned. The reaching of the current control objective matches the higher oscillating

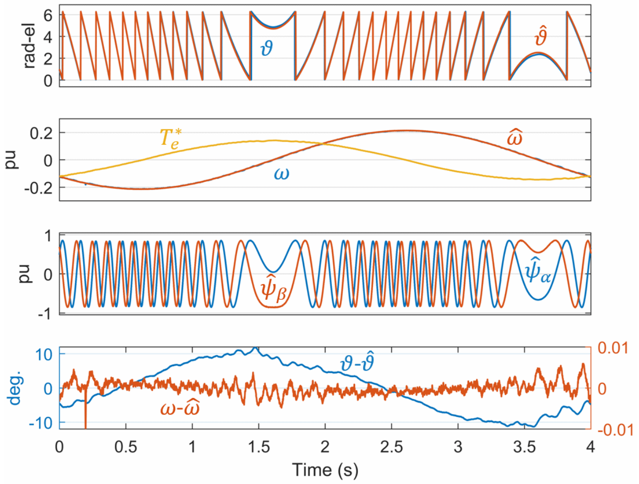

FIGURE 20. **CDAF at 100% of rated value.**

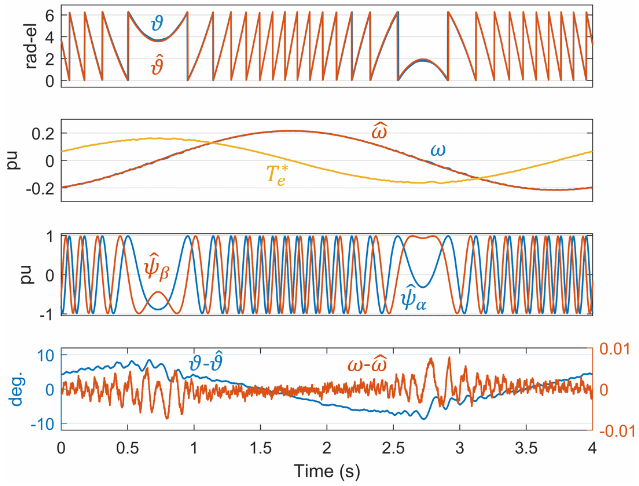

FIGURE 21. **CDAC control at 100% of rated value.**

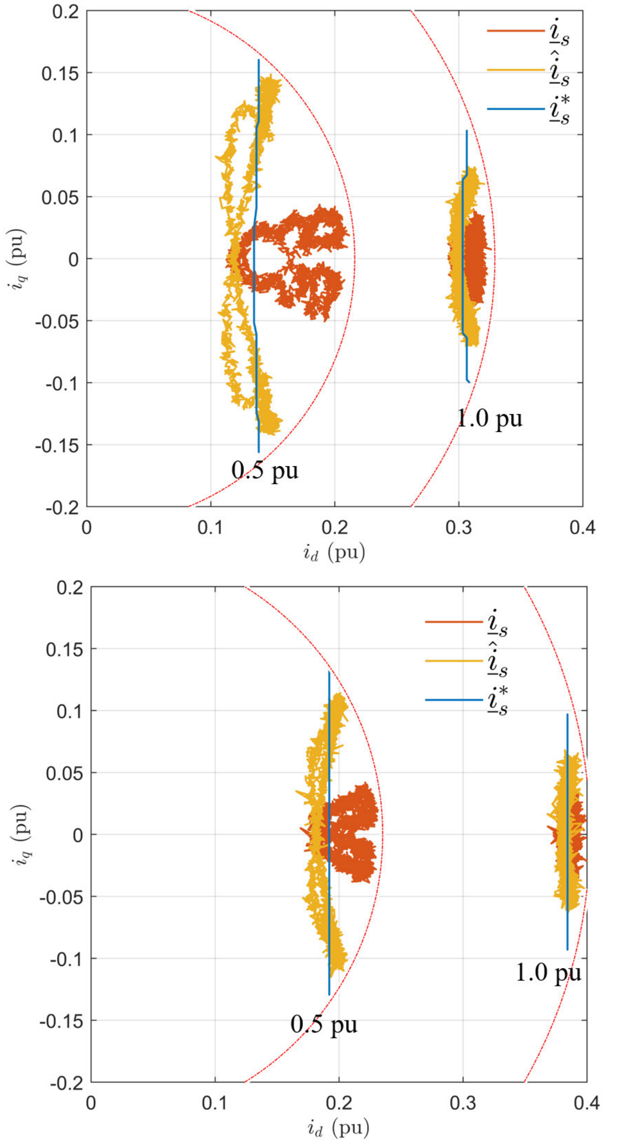

FIGURE 22. **Comparison of CDAF (above) and CDAC (below) control loci.**

contents of the estimates (see estimated speed, position, and estimation errors in Figures 20 and 21).

The sinusoidal speed reference test presented up to now does not involve the operation close to the origin of the torque-speed plane, i.e., with contemporary low torque and speed. Hence, the different current control strategies have been tested by constant speed reference at no-load and the lowest speed operating limit has been detected. The results are presented in Figures from 24 to 28.

The lowest speed limit of the MTPA/ME control, Figure 24, is around 150 rpm (0.1 *p.u.*), the speed estimate is acceptable and regular during the inversion but the steady-state position error is excessively large (50 deg. on average) and compromises the field-orientation logic itself: in fact, the speed is negative with positive torque command and not-zero current (i.e. flux) operation is reached at non load. When the speed reversion is commanded, large oscillations are triggered with long recovery time. Nevertheless, the estimates are about constant at steady state, that is a reflex of the poor control stiffness (the actual torque/to/current ratio is poor due to the detuning).

The CDAF control at 50% of the rated value, Figure 25, performs better: it reaches a lower speed limit of around 60 rpm (0.04 *p.u.*), the recovery time of the oscillations due to the reversion is much shorter and the steady-state (average) position error smaller (about 10 deg.).

A still better behavior is achieved by the CDAC control at 50% of the rated value, Figure 26. It reaches about the same minimum speed of the CDAC (60 rpm) and same value of the average estimation error, but the oscillation peaks are lower and the overall response shapes more regular.

Finally, Figures 27 and 28 show the results with CDAF and CDAC at 100% of the rated values, respectively. Both reach the very low operating speed of 15 rpm (0.01 *p.u.*), comparable with the intrinsic measurement noise of the speed

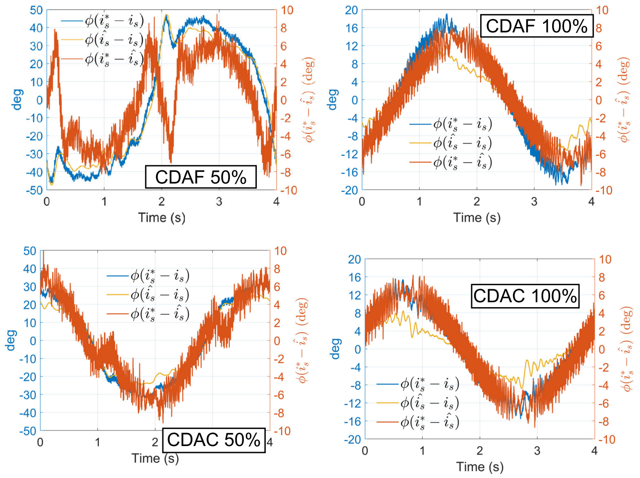

FIGURE 23. Sensorless control errors of CDAF and CDAC.

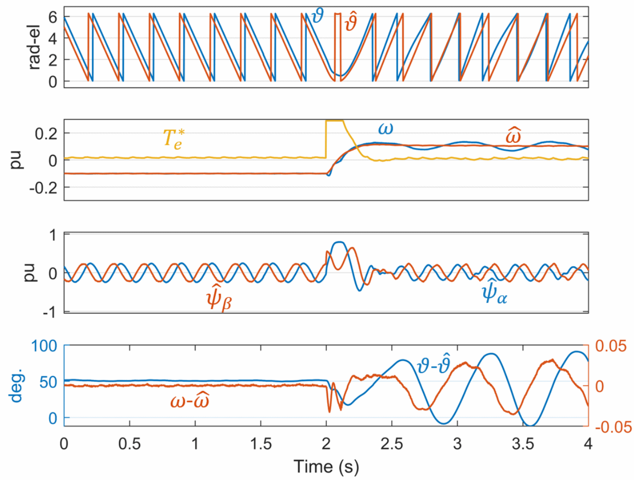

FIGURE 24. MTPA/ME control: lowest limit operating speed (150RPM) with reversion.

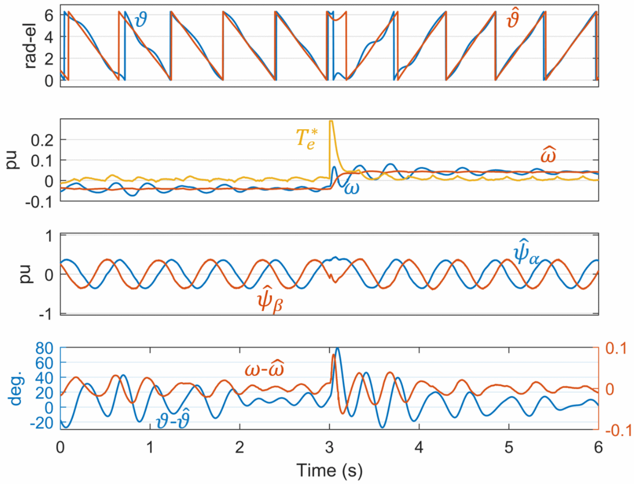

FIGURE 25. CDAF control at 50% of rated value: lowest limit operating speed (60 RPM) with reversion.

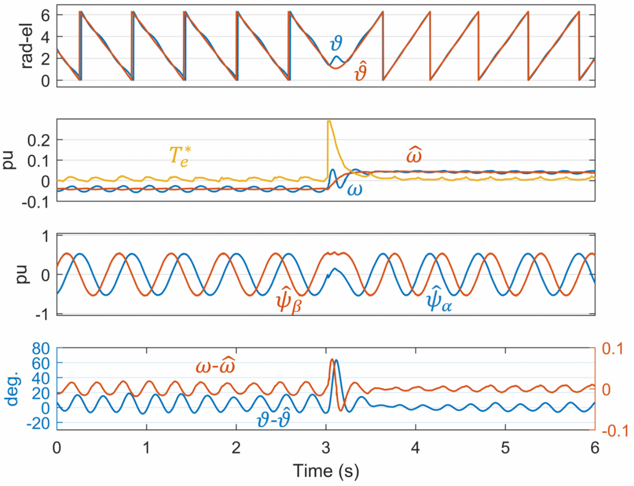

FIGURE 26. CDAC control at 50% of rated value: lowest limit operating speed (60 RPM) with reversion.

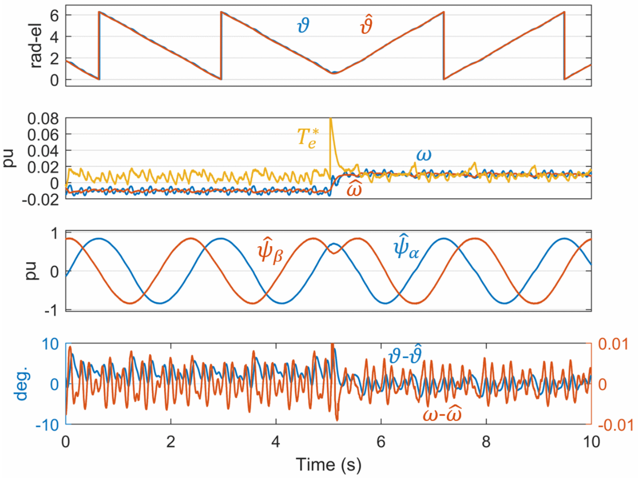

FIGURE 27. CDAF control at 100% of rated value: lowest limit operating speed (15 RPM) with reversion.

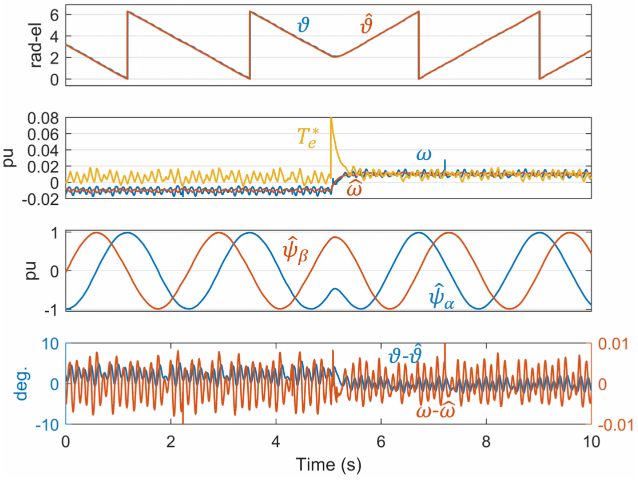

FIGURE 28. CDAC control at 100% of rated value: lowest limit operating speed (15 RPM) with reversion.

sensor (actually the speed estimate signal is less noisy than the speed measure). The average position error is limited to few degrees (about 3 deg. at most) and it does not exceed 10 deg. at reversion. The good field orientation allows to achieve the designed stiffness of the control and observers loops (resulting in an increased frequency of the oscillation of the estimates).

The responses of the CDAC and CDAF at 100% are very similar, nevertheless the CDAC (i.e., when the flux imposed is higher) behaves slightly better.

VI. CONCLUSION

In this paper, a flux observer for speed sensorless field-oriented control of SynRel motors has been investigated with several current strategies, specifically maximum torque per ampere (MTPA), maximum efficiency (ME), maximum power factor (MPF), constant direct-axis-current (CDAC) and constant direct-axis-flux (CDAF).

The results highlight the importance of the selection of the control strategies to improve the quality of the sensorless control, in particular:

- the flux observer requires a minimum flux value for the estimation, and it is sensitive to its variations: MTPA, ME and MPF control strategies does not match these requirements and their application is critical;
- CDAC and CDAF controls meet the minimum flux requirement but the choice of the minimum current level or respectively flux to apply becomes very important;
- the higher is the flux/current operating level, the better is the sensorless control performance: CDAF and CDAC at 100% of the rated values are the best in this regard but, obviously, these conditions may not be acceptable at low load (and speed) conditions or when maximum efficiency is involved.

The analysis of the convergence properties of the sensorless control is beyond the scope of the present paper. Nevertheless, the flux-observer has proven its effectiveness and the control strategy can be properly tailored to given applications. In facts, also the maximizing performance controls MTPA, ME, and MPF might be used by working with a minimum flux or a minimum current set according to the operating load/speed conditions. These topics will be matters of further studies.

REFERENCES

[1] I. Boldea, L. N. Tutelea, L. Parsa, and D. Dorrell, "Automotive electric propulsion systems with reduced or no permanent magnets: An overview," *IEEE Trans. Ind. Electron.*, vol. 61, no. 10, pp. 5696–5711, Oct. 2014.

[2] A. Vagati, "The synchronous reluctance solution: A new alternative in AC drives," in *Proc. IECON 20th Annu. Conf. IEEE Ind. Electron.*, Sep. 1994, pp. 1–13.

[3] A. Credo, G. Fabri, M. Villani, and M. Popescu, "Adopting the topology optimization in the design of high-speed synchronous reluctance motors for electric vehicles," *IEEE Trans. Ind. Appl.*, vol. 56, no. 5, pp. 5429–5438, Sep. 2020.

[4] J. Park, C. Kalev, and H. F. Hofmann, "Control of high-speed solid-rotor synchronous reluctance motor/generator for flywheel-based uninterruptible power supplies," *IEEE Trans. Ind. Electron.*, vol. 55, no. 8, pp. 3038–3046, Aug. 2008.

[5] S. Taghavi and P. Pillay, "A sizing methodology of the synchronous reluctance motor for traction applications," *IEEE J. Emerg. Sel. Topics Power Electron.*, vol. 2, no. 2, pp. 329–340, Jun. 2014.

[6] M. Ferrari, N. Bianchi, A. Doria, and E. Fornasiero, "Design of synchronous reluctance motor for hybrid electric vehicles," *IEEE Trans. Ind. Appl.*, vol. 51, no. 4, pp. 3030–3040, Jul. 2015.

[7] E. Howard, M. J. Kamper, and S. Gerber, "Asymmetric flux barrier and skew design optimization of reluctance synchronous machines," *IEEE Trans. Ind. Appl.*, vol. 51, no. 5, pp. 3751–3760, Sep./Oct. 2015.

[8] A. Credo, G. Fabri, M. Villani, and M. Popescu, "A robust design methodology for synchronous reluctance motors," *IEEE Trans. Energy Convers.*, vol. 35, no. 4, pp. 2095–2105, Dec. 2020.

[9] A. Credo, A. Cristofari, S. Lucidi, F. Rinaldi, F. Romito, M. Santececca, and M. Villani, "Design optimization of synchronous reluctance motor for low torque ripple," in *A View of Operations Research Applications in Italy* (AIRO Springer Series), 2019, pp. 53–69, doi: 10.1007/978-3-030-25842-9_5.

[10] G. Pellegrino, F. Cupertino, and C. Gerada, "Automatic design of synchronous reluctance motors focusing on barrier shape optimization," *IEEE Trans. Ind. Appl.*, vol. 51, no. 2, pp. 1465–1474, Mar./Apr. 2015.

[11] L. Xu, X. Xu, T. A. Lipo, and D. W. Novotny, "Vector control of a synchronous reluctance motor including saturation and iron loss," *IEEE Trans. Ind. Appl.*, vol. 27, no. 5, pp. 977–985, Sep. 1991.

[12] R. E. Betz, R. Lagerquist, M. Jovanovic, T. J. E. Miller, and R. H. Middleton, "Control of synchronous reluctance machines," *IEEE Trans. Ind. Appl.*, vol. 29, no. 6, pp. 1110–1122, Nov. 1993.

[13] K. Malekian, M. R. Sharif, and J. Milimonfared, "An optimal current vector control for synchronous reluctance motors incorporating field weakening," in *Proc. 10th IEEE Int. Workshop Adv. Motion Control*, Mar. 2008, pp. 393–398.

[14] A. E. Hoffer, R. H. Moncada, B. J. Pavez, J. A. Tapia, and L. Laurila, "A high efficiency control strategy for synchronous reluctance generator including saturation," in *Proc. 22nd Int. Conf. Electr. Mach. (ICEM)*, Sep. 2016, pp. 39–45.

[15] W. T. Villet and M. J. Kamper, "Variable-gear EV reluctance synchronous motor drives—An evaluation of rotor structures for position-sensorless control," *IEEE Trans. Ind. Electron.*, vol. 61, no. 10, pp. 5732–5740, Oct. 2014.

[16] A. Consoli, G. Scarcella, G. Scelba, A. Testa, and D. A. Triolo, "Sensorless rotor position estimation in synchronous reluctance motors exploiting a flux deviation approach," *IEEE Trans. Ind. Appl.*, vol. 43, no. 5, pp. 1266–1273, Sep. 2007.

[17] S.-J. Kang, J.-M. Kim, and S.-K. Sul, "Position sensorless control of synchronous reluctance motor using high frequency current injection," *IEEE Trans. Energy Convers.*, vol. 14, no. 4, pp. 1271–1275, Dec. 1999.

[18] T. Tuovinen and M. Hinkkanen, "Adaptive full-order observer with high-frequency signal injection for synchronous reluctance motor drives," *IEEE J. Emerg. Sel. Topics Power Electron.*, vol. 2, no. 2, pp. 181–189, Jun. 2014.

[19] S.-C. Agarlita, I. Boldea, and F. Blaabjerg, "High-frequency-injection-assisted 'active-flux'-based sensorless vector control of reluctance synchronous motors, with experiments from zero speed," *IEEE Trans. Ind. Appl.*, vol. 48, no. 6, pp. 1931–1939, Nov./Dec. 2012.

[20] F. J. W. Barnard, W. T. Villet, and M. J. Kamper, "Hybrid active-flux and arbitrary injection position sensorless control of reluctance synchronous machines," *IEEE Trans. Ind. Appl.*, vol. 51, no. 5, pp. 3899–3906, Sep. 2015.

[21] A. Stirban, I. Boldea, and G.-D. Andreescu, "Motion-sensorless control of BLDC-PM motor with offline FEM-information-assisted position and speed observer," *IEEE Trans. Ind. Appl.*, vol. 48, no. 6, pp. 1950–1958, Nov. 2012.

[22] M. Hinkkanen, P. Pescetto, E. Molsa, S. E. Saarakkala, G. Pellegrino, and R. Bojoi, "Sensorless self-commissioning of synchronous reluctance motors at standstill without rotor locking," *IEEE Trans. Ind. Appl.*, vol. 53, no. 3, pp. 2120–2129, May 2017.

[23] P. Pescetto and G. Pellegrino, "Sensorless magnetic model and PM flux identification of synchronous drives at standstill," in *Proc. IEEE Int. Symp. Sensorless Control Electr. Drives (SLED)*, Sep. 2017, pp. 79–84.

[24] T. Kojima, T. Suzuki, M. Hazeyama, and S. Kayano, "Position sensorless control of synchronous reluctance machines based on magnetic saturation depending on current phase angles," *IEEE Trans. Ind. Appl.*, vol. 56, no. 3, pp. 2171–2179, Jan. 2020.

[25] M. Tursini, A. Credo, G. Fabri, F. Parasiliti, and M. Villani, "Assessment of control strategies for synchronous reluctance motors," in *Proc. Int. Conf. Energy Efficiency Motor Driven Syst. (EEMODS)*, Rome, Italy, Sep. 2017, pp. 759–772.

[26] M. Tursini, M. Villani, G. Fabri, S. Paolini, A. Credo, and A. Fioravanti, "Sensorless control of a synchronous reluctance motor by finite elements model results," in *Proc. IEEE Int. Symp. Sensorless Control Electr. Drives (SLED)*, Sep. 2017, pp. 19–24.

[27] M. Tursini, M. Villani, G. Fabri, A. Credo, F. Parasiliti, and A. Abdelli, "Synchronous reluctance motor: Design, optimization and validation," in *Proc. Int. Symp. Power Electron., Electr. Drives, Autom. Motion (SPEEDAM)*, Jun. 2018, pp. 1297–1302.

[28] H. A. A. Awan, T. Tuovinen, S. E. Saarakkala, and M. Hinkkanen, "Discrete-time observer design for sensorless synchronous motor drives," *IEEE Trans. Ind. Appl.*, vol. 52, no. 5, pp. 3968–3979, Sep. 2016.

[29] A. Yousefi-Talouki, P. Pescetto, G. Pellegrino, and I. Boldea, "Combined active flux and high-frequency injection methods for sensorless direct-flux vector control of synchronous reluctance machines," *IEEE Trans. Power Electron.*, vol. 33, no. 3, pp. 2447–2457, Mar. 2018.

[30] T. Tuovinen, M. Hinkkanen, and J. Luomi, "Analysis and design of a position observer with resistance adaptation for synchronous reluctance motor drives," *IEEE Trans. Ind. Appl.*, vol. 49, no. 1, pp. 66–73, Jan. 2013.

[31] A. Varatharajan and G. Pellegrino, "Sensorless synchronous reluctance motor drives: A projection vector approach for stator resistance immunity and parameter adaptation," *IEEE Trans. Ind. Appl.*, vol. 56, no. 5, pp. 5003–5012, Sep./Oct. 2020.

[32] L. D. Tornello, G. Scelba, G. Scarcella, M. Cacciato, A. Testa, S. Foti, S. de Caro, and M. Pulvirenti, "Combined rotor-position estimation and temperature monitoring in sensorless, synchronous reluctance motor drives," *IEEE Trans. Ind. Appl.*, vol. 55, no. 4, pp. 3851–3862, Jul. 2019.

[33] A. Fratta and A. Vagati, "A reluctance motor drive for high dynamic performance application," *IEEE Trans. Ind. Appl.*, vol. 28, no. 4, pp. 873–979, Jul./Aug. 1992.

[34] M. Bilewski, A. Fratta, L. Giordano, A. Vagati, and F. Villata, "Control of high-performance interior permanent magnet synchronous drives," *IEEE Trans. Ind. Appl.*, vol. 29, no. 2, pp. 328–337, Mar. 1993.

[35] A. Vagati, M. Pastorelli, and G. Franceschini, "High-performance control of synchronous reluctance motors," *IEEE Trans. Ind. Appl.*, vol. 33, no. 4, pp. 983–991, Aug. 1997.

[36] P. Pescetto and G. Pellegrino, "Sensorless standstill commissioning of synchronous reluctance machines with automatic tuning," in *Proc. IEEE Int. Electr. Mach. Drives Conf. (IEMDC)*, May 2017, pp. 1–8.

[37] H. Mahmoud, G. Bacco, M. Degano, N. Bianchi, and C. Gerada, "Synchronous reluctance motor iron losses: Considering machine nonlinearity at MTPA, FW, and MTPV operating conditions," *IEEE Trans. Energy Convers.*, vol. 33, no. 3, pp. 1402–1410, Sep. 2018.

[38] S. Piriienko, U. Ammann, M. Neuburger, F. Bertele, T. Roser, A. Balakhontsev, N. Neuberger, and P.-W. Cheng, "Influence of the control strategy on the efficiency of SynRM based small-scale wind generators," in *Proc. IEEE Int. Conf. Ind. Technol. (ICIT)*, Feb. 2019, pp. 280–285.

[39] P. R. Ghosh, A. Das, and G. Bhuvaneswari, "Performance comparison of different vector control approaches for a synchronous reluctance motor drive," in *Proc. 6th Int. Conf. Comput. Appl. Electr. Eng.-Recent Adv. (CERA)*, Oct. 2017, pp. 320–325.

[40] A. Yousefi-Talouki, P. Pescetto, and G. Pellegrino, "Sensorless direct flux vector control of synchronous reluctance motors including standstill, MTPA, and flux weakening," *IEEE Trans. Ind. Appl.*, vol. 53, no. 4, pp. 3598–3608, Jul. 2017.

[41] *Sensorless Control of Synchronous Reluctance Motor by Flux Observer [Video]. YouTube*. Accessed: Jun. 16, 2021. [Online]. Available: https://youtu.be/U-ofHSdmhCg

ANDREA CREDO received the B.Sc. and M.Sc. degrees (Hons.) in electrical engineering and the Ph.D. degree *(cum laudem)* from the University of L'Aquila, L'Aquila, Italy, in 2015, 2017, and 2021, respectively. He currently works as a Research Assistant with the University of L'Aquila. His research interests include the design and the control of synchronous reluctance motor. He received the ICEM Jorma Luomi Student Forum Award during the ICEM 2020 in Gothenburg, Sweden (Virtual Conference).

LINO DI LEONARDO was born in Pescina, Italy, in October 1986. He received the M.S. degree in computer and automation engineering, in 2010, and the Ph.D. degree in electrical and information engineering from the University of L'Aquila, in 2014. In 2012, he was a Visiting Ph.D. Student at the École Supérieure d'Ingénieurs en Électrotechnique et Électronique d'Amiens (ESIEE-Amiens). He currently works as an Assistant Researcher with the Department of Industrial and Information Engineering and Economics, University of L'Aquila. In particular, his Ph.D. thesis concerns dynamic co-simulation analysis of motor drives. His research interests include design, modeling, and simulation of electrical machines with focus on permanent-magnet synchronous motors, dual-rotor permanent magnet induction machine, and reluctance motors. He has experience with finite-element and multi-physics integrated simulation tools along with DSP-based real-time simulation platforms.

FRANCESCO PARASILITI COLLAZZO received the M.S. degree in electrical engineering from the Sapienza University of Rome, Italy, in 1981. In 1983, he joined the Department of Electrical Engineering, University of L'Aquila, Italy, as an Assistant Professor. From 1992 to 1999, he was an Associate Professor of electrical drives at the University of L'Aquila. Since 2000, he has been a Full Professor at the University of L'Aquila, where he was the Head of the Department of Industrial and Information Engineering and Economics, from 2012 to 2018. His studies deal with design optimization of induction, PM synchronous and reluctance motors, modeling and parameter observation of induction and synchronous machines, and digital control of electrical drives. Since 2004, he has been a member of the Steering Committee of the International Conference on Electrical Machines (ICEM). From 2010 to 2019, he was the Vice-Chair of the ICEM Steering Committee. He is currently the Chair of the ICEM Administrative Committee (Ex-Steering Committee).

MARCO TURSINI (Member, IEEE) was born in L'Aquila, Italy, in 1960. He received the M.S. degree in electrical engineering from the University of L'Aquila, L'Aquila, in 1987. In 1987, he joined the Department of Electrical Engineering, University of L'Aquila, as an Associate Researcher. He became an Assistant Professor of power converters, electrical machines, and drives, in 1991, and a Full Professor, in 2017. In 1990, he was a Research Fellow with the Industrial Electronics Laboratory, Swiss Federal Institute of Technology, Lausanne, Switzerland, where he conducted research on sliding-mode control of permanent-magnet synchronous motor drives and, in 1994, with Nagasaki University, Nagasaki, Japan. Since 1990, he has been taking the responsibility of several national research projects and contracts between the University of L'Aquila and industrial partners. He has authored more than 150 technical papers on these subjects. His research interests include advanced control of ac drives, including vector and sensorless control, multiphase motors and drives, digital motion control, DSP-based systems for real-time implementation, and modeling and simulation of electrical drives.

• • •